AIAA 97-2478

Aeroheating and Aerodynamic CFD Validation And Prediction For The X-38 Program

Mark P. Loomis
NASA-Ames Research Center
Moffett Field CA

Ethiraj Venkatapathy, Periklis Papadopoulos
Thermosciences Institute
Moffett Field CA

Carol B. Davies
Sterling Software, NASA Ames Division
Moffett Field CA

Scott Berry, Tom Horvath
NASA Langley Research Center, Hampton VA

Charles Campbell
NASA Johnson Space Center
Houston TX

32nd Thermophysics Conference
June 23 - 25, 1997 / Atlanta, GA

For permission to copy or republish, contact the American Institute of Aeronautics and Astronautics
1801 Alexander Bell Drive, Suite 500, Reston, VA 22091

AEROHEATING AND AERODYNAMIC CFD VALIDATION AND PREDICTION FOR THE X-38 PROGRAM

Mark P. Loomis *
NASA Ames Research Center, Moffett Field CA 94035

Ethiraj Venkatapathy,† Periklis Papadopoulos ‡
Thermosciences Institute, Moffett Field CA 94035

Carol B. Davies §
Sterling Software, Moffett Field CA 94035

Scott Berry¶, Tom Horvath¶
NASA Langley Research Center, Hampton VA 23681

Charles Campbell #
NASA Johnson Space Center, Houston TX 77058

Abstract

This paper presents the results of a computational fluid dynamics validation exercise using the General Aerodynamic Simulation Program (GASP) code for vehicles under consideration for the X-38 program. The scope of the exercise involved simulation and comparison with wind tunnel aeroheating and aerodynamic data in the hypersonic regime. In addition, simulations were performed and results are presented for the full-scale flight vehicle along an expected re-entry trajectory.

Nomenclature

C_A	=	axial force coefficient, $F_A/ q_\infty S_{ref}$
C_m	=	moment coefficient, $m/ q_\infty S_{ref} L$
C_N	=	normal force coefficient, $F_N/ q_\infty S_{ref}$
C_p	=	pressure coefficient $(p-p_\infty)/q_\infty$
h	=	heat-transfer coefficient
h_{ref}	=	reference heat-transfer coefficient
F_A	=	axial force, lb_f
F_N	=	normal force, lb_f
L	=	reference length, 276 in
L_x	=	streamwise reference length, 282.5 in
L_y	=	spanwise reference length, 86.75 in
m	=	moment, ft-lb_f
M	=	Mach number
p	=	static pressure, psf
p_∞	=	free-stream static pressure, psf
q_{ref}	=	reference heating rate, BTU/ft^2-sec
q_w	=	heat transfer to the wall, BTU/ft^2-sec
q_∞	=	free-stream dynamic pressure, psf
$Re_{\infty,L}$	=	free-stream Reynolds number
Re_∞	=	free-stream unit Reynolds number, ft^{-1}
S_{ref}	=	reference area, 23.328 in^2
T_w	=	wall temperature, deg F
x	=	axial coordinate, in
X_{ref}	=	moment reference x location, 157.32 in
y	=	spanwise coordinate, in
z	=	normal coordinate, in
Z_{ref}	=	moment reference z location, 26.386 in
α	=	angle of attack, deg
δ_{bf}	=	body-flap deflection, deg

Introduction

X-38 Description:
The goal of the X-38 program is to flight test and demonstrate an experimental Crew Return Vehicle capable of returning International Space Station (ISS) crew members safely to Earth in the event of an emergency. The vehicle shape is a derivative of the X-23 and X-24A lifting body configurations which were flown in the late 1960's and early 1970's. The lifting body (see Fig. 1) configuration was initially chosen because its cross range capability leads to a shorter on-orbit loiter time compared to a blunt body concept such as the Apollo return capsule. The shorter loiter time was considered an important design goal in the event of a medical emergency; the crew members must be returned to safety as soon as possible. The design was established by a team of engineers at NASA Johnson

* Aerospace Engineer, Reacting Flow Environments Branch
† Director of Research, ELORET, Senior Member AIAA
‡ Senior Research Scientist, ELORET, Member AIAA
§ Research Specialist, Member AIAA
¶ Aerospace Engineer, Aerothermodynamics Branch
# Aerospace Engineer, Aerosciences Branch, Member AIAA

Copyright © 1997 by the American Institute of Aeronautics and Astronautics, Inc. No copyright is asserted in the United States under Title 17, U.S. Code. The U.S. Government has a royalty-free license to exercise all rights under the copyright claimed herein for Governmental Purposes. All other rights are reserved by the copyright owner.

Space Center with the philosophy of using demonstrated, but not necessarily flight proven, technologies.[1]

The baseline vehicle dimensions (Revision 3.1 geometry) are 24 ft in length with a wingspan of just under 14 ft and was designed to return four crew members. The program has evolved and the baseline geometry has been scaled up to 120% of the original version to accommodate six crew members. A collaborative effort between NASA and ESA to improve the vehicle volumetric and structural performance and satisfy Crew Transfer Vehicle (CTV) needs has resulted in changes to the flight vehicle geometry. However, these changes are predominantly on the leeside of the vehicle and hence are not expected to be significant in the hypersonic flight regime.

As part of the vehicle design effort, an aerothermodynamic heating definition methodology[1] provided the baseline data used to design the thermal protection system. This methodology used a two-layer inviscid-boundary layer code approach. Recently, Computational Fluid Dynamics (CFD) codes and computer hardware advancements have evolved to a point where solutions of the full Navier-Stokes equations can be used in a timely and accurate manner in the vehicle design process for the prediction of trajectory-based aerothermal environments.[2]

The hypersonic aerothermodynamic database for this vehicle relies on an extensive number of runs in ground-based hypersonic facilities.[3,4,5] Although these facilities are able to match important variables such as Mach number and Reynolds number, they are unable to reproduce the real-gas effects associated with the high temperature, chemically-reacting nature of the flow field during entry. These real-gas effects have been shown in the past to cause discrepancies in predicted parameters such as the pitching moment,[6] which is important for establishing vehicle trim. Real-gas CFD solvers, once properly validated, are used to extrapolate the design database to real flight conditions. Results from the GASP solver have previously been compared with Space Shuttle Orbiter flight data during entry.[7] These calculations, validated with ground-based results for a specific geometry and verified against flight data from similar missions, then form the backbone of the design database.

A key requirement for the incorporation of CFD into the database is proper validation using available experimental data. This paper presents the results of a validation exercise using the GASP[8] CFD code to predict both aerothermal heating and aerodynamic characteristics in the hypersonic regime for vehicles with geometries under consideration for the X-38 program.

CFD Solution Methodology

The CFD code used in this work is the General Aerodynamics Simulation Program (GASP v3.0).[8] The code solves the full Navier-Stokes equations including species equations for thermochemistry with a finite-volume spatial discretization. A number of different thermochemical models exist. In this work, perfect-gas models for air and helium are used in the wind tunnel validation exercises. A 5-species (N_2, O_2, NO, N, O) finite-rate chemistry air model using Park's[9] reaction rates is used for the flight cases. The transport properties are calculated with Wilke's[10] mixing rule with curve fits for the species viscosities given by Blottner, et al.,[11] Eucken's correlation for thermal conductivity, and binary diffusion with a constant Schmidt number of 0.8. The third-order Van Leer flux splitting scheme with the min-mod limiter is used to calculate the inviscid fluxes and a central-difference approximation is used for the viscous fluxes. The discretized system of equations can be solved in many different ways, such as using point-Jacobi, Gauss-Seidel, or two-factor ADI. These methods have similar accuracy but the choice of the method may affect convergence. Typically, two-factor ADI is used for these calculations.

Boundary Conditions

For the wind tunnel simulations, a fixed-wall temperature boundary condition is imposed. For the flight cases, a radiative equilibrium, fully catalytic wall boundary condition with a constant emissivity of 0.85 is imposed for most calculations. In some cases, the surface catalysis for TUFI coated tiles is modeled using a first order reaction rate with curve fits from Ref. 12. For all cases, the body-flap gap region is modeled as a simple outflow boundary condition with a low imposed back pressure to avoid issues related to baseflow / gap flow interactions.

Grid Generation

Grids were generated with the GRIDGEN[13] and HYPGEN[14] software packages. The nominal grid consists of 81 points in the streamwise direction, 93 points circumferentially, and 61 points in the normal direction. Care was taken to assure grid orthogonality and smoothness on the surface. An initial solution was obtained on a grid that is much larger than the shock envelope. As a result, the code OUTBOUND, an offshoot of the SAGE[15] code, is used to adapt and move the outer boundary near the shock and to recluster the body-normal points in the boundary layer. This procedure ensures that grid points are used in an efficient manner. Instead of generating grids for each angle-of-attack separately, the original grid is adapted to each case and thereby the time spent to generate

grids is reduced significantly. A schematic of the surface grid is seen in Figure 1.

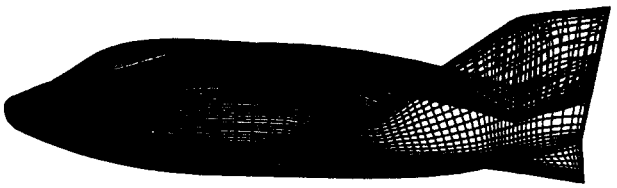

Figure 1. X-38 Geometry and computational surface grid topology.

Solution Strategy and Computational Requirements
The solutions are run employing a mesh sequencing technique, i.e. solutions are obtained on an initial coarse grid and interpolated onto progressively finer grids. This procedure drastically decreases the time to converge the finest sequence since the final solution is initialized with a very good initial approximation. In addition, the overall time to converge the solution is decreased since the iterations take much less time per step on the coarse grids. Convergence of the finest sequence requires typically less than 400 steps.

The solutions are obtained on a six processor SGI Power Challenge L (based on the MIPS R8000 microprocessor) workstation. Utilizing a single processor, the perfect gas simulations on the nominal (81 x 93 x 61) grid require approximately 16 hours to converge while the reacting gas cases take approximately 80 hours. In terms of equivalent Cray C90 CPU time, the perfect gas solutions require about 3 hours and the real gas cases require 12 hours. Memory requirement were 9 MW for the perfect gas cases and 14 MW for the real gas solutions. The limited CPU time and memory requirements make the code a fast and efficient design tool.

Grid Refinement Strategy and Results

To establish error metrics and to demonstrate the dependency of the solution quality on the choice and distribution of the grid points and on the numerical solvers, a number of simulations are performed and the results are detailed below. These numerical experiments are performed to ensure that the computed CFD solutions are grid independent. The conditions correspond to those of the wind tunnel test in Table 2 for which aeroheating data was available. Similar studies were performed to demonstrate that the grid was sufficient to resolve the aerodynamic forces but are not presented.

Effect of Axial and Circumferential Refinement
The effect of progressively finer grids in the axial and circumferential directions is shown in Fig. 2a, which is a plot of the surface heat flux on a constant circumferential grid line that starts at the nose and passes through the middle of the flap on the windward side. The initial wall spacing is set to 3 microns which corresponds to a maximum wall-cell Reynolds number on the order of 2-3. It is seen that in most areas the coarse-grid (41 x 47 x 61) solution is very close to the finest-grid (161 x 185 x 61) solution. The largest difference occurs in the flap region which consists of a complex separated flow field. Figure 2b shows the effect of the different grids along a constant axial grid line that runs from the windward to leeward side. Again a very small difference is seen. Assuming that the finest grid provides the most accurate solution, an error estimate is made from the coarser grid solution and this is shown in Fig. 2c. Based on this, it was decided that the nominal grid (81 x 93 x 61) was sufficient to resolve the aeroheating in the axial and streamwise directions. However, the (41 x 47 x 61) grid provides a very good prediction for acreage calculations.

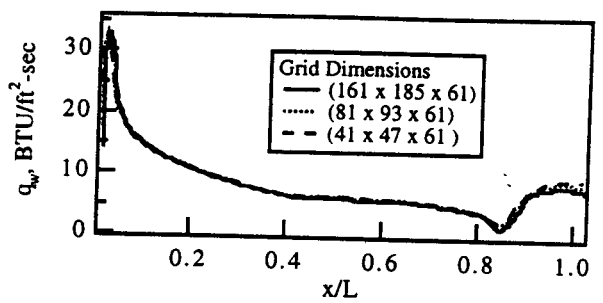

Figure 2a. Effect of axial and circumferential refinement - windward side heat flux.

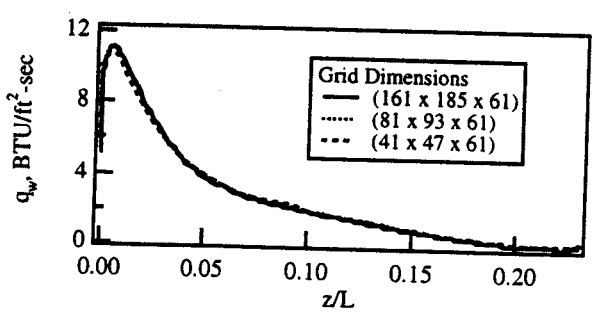

Figure 2b. Effect of axial and circumferential refinement - heat flux along an axial cut (x/L=0.5).

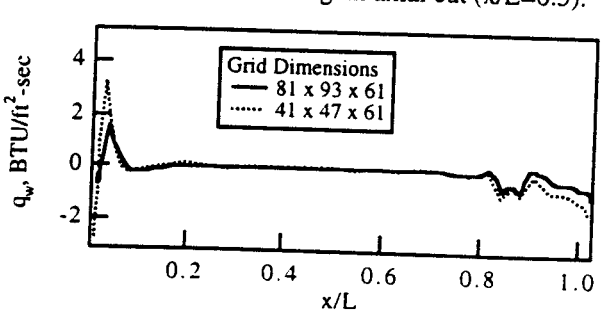

Figure 2c. Error in windward side heat-flux prediction.

Number of Points in the Normal Direction

The effect of the number of points in the normal direction is shown in Fig. 3 which is a plot of the windward centerline heat transfer. Cases are run with 31, 51, 61 and 121 points in the normal direction. To save time only the forebody is included in the study. The results show a significant overprediction of heat transfer with only 31 points, however the grids with 51 or 61 points produce values that are much closer to the 121-point case. The error in heat-transfer prediction between the 61-point grid and the 121-point grid is no more than 1 BTU/ft^2-sec and occurs near the singular point at the nose. Based on this study it was decided that 61 points in the normal direction is sufficient.

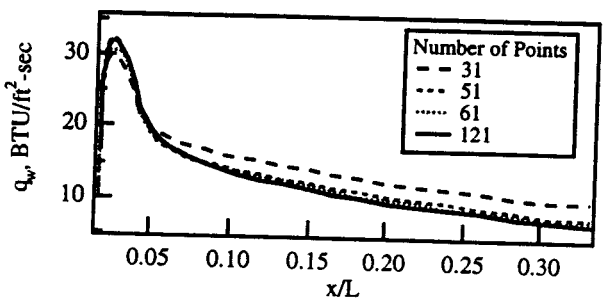

Figure 3. Grid refinement study, effect of number of points in the normal direction.

Effect of Wall Spacing

The effect of the initial wall spacing is shown in Fig. 4 for the nominal grid. The nominal grid spacing is 3 microns which corresponds to a maximum cell Reynolds number of about 2-3. The remaining grid points were stretched in the normal direction according to the reclustering algorithm in the OUTBOUND[15] code. It can be seen that the predicted heat transfer changes no more than 1 BTU/ft^2-sec with a factor of three change in cell Reynolds number. However, a large wall spacing, especially at the nose, has the effect of increased heat transfer.

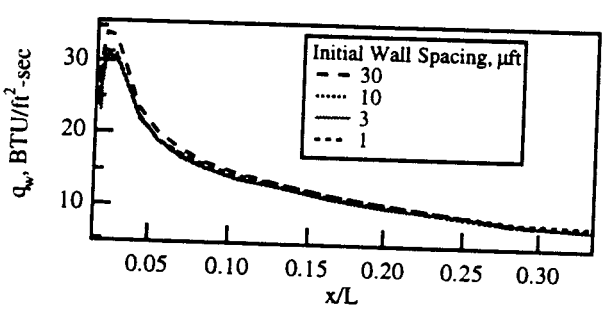

Figure 4. Effect of wall spacing on heat transfer.

Thus, a wall spacing with a cell Reynolds number no greater than 5, combined with smooth stretching from the wall to the shock with 61 grid points, is shown to provide sufficient solution accuracy.

Convergence Studies

The time-step determination for solving the unsteady Navier-Stokes equations within the GASP solver is based on either local or global flow conditions.[8] The best convergence is usually found with a combination of the two. Figure 5 is the plot of the L_2 norm of the residual versus the number of iterations for two cases on the nominal grid (81 x 93 x 61). In Case 1, the CFL is ramped from 0.1 to 1.5 for 50 steps and then held constant at 1.5 for 50 more steps. Over the next 50 steps the CFL is again ramped from 0.1 to 1.5 using the local time-step option. The solution then converges using a constant value of 1.5 with the local option. This combination produces a fast, stable path to convergence for this class of problems.

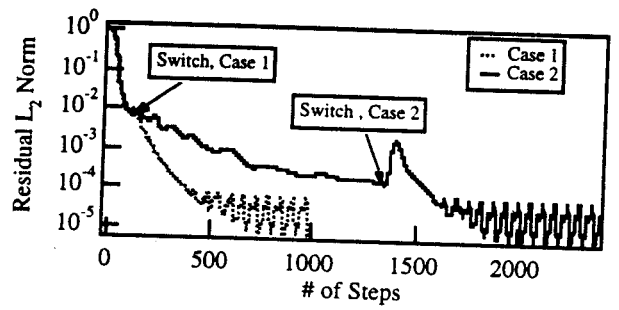

Figure 5. L2 norm of residual vs. number of steps.

As is seen in Fig. 5, the residual L2 norm drops over four orders of magnitude and then oscillates. Figure 6 shows a plot of the calculated heat transfer after a number of steps for Case 1 along a line on the windward side slightly off centerline. It is seen that, in terms of surface heat transfer, after 200 iterations the solution is reasonably close to the 1000-iterations solution, which is assumed to be the converged solution. In terms of percentage differences, after 200 steps the solution is converged to within less than 1%, except in the flap region. This corresponds to a drop in the residual of 3 orders of magnitude. After 400 steps the residual has dropped 4 orders and the solution is within less than 1% of the final solution everywhere.

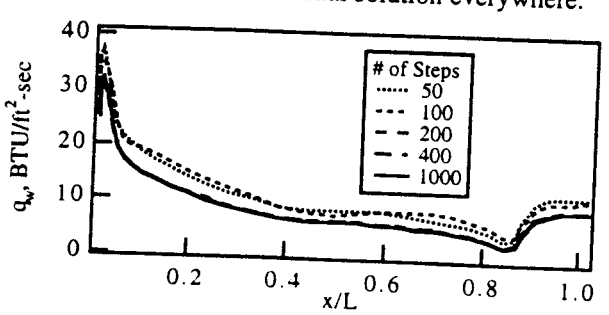

Figure 6. Evolution of the windward side heat flux as a function of iterations.

The advantage of utilizing the local time-stepping option is illustrated by comparison with Case 2, in

which many more steps are run with the global option. Figure 5 clearly shows the residual dropping more slowly for Case 2 than Case 1, where the switch to local time stepping occurs after only 100 iterations. Even after 1300 steps, the residual has not converged in Case 2 and the heat transfer still differs from the converged value by 5-10%. Once the CFL is switched to the local value, the residual initially increases, then rapidly converges and the heat transfer approaches the converged solution.

Summary of Hypersonic Ground Test Data

The X-38 hypersonic ground test program consists of data from several different facilities at NASA Langley Research Center, as summarized in Table 1. Details are found in Refs. 3-5. The aerodynamic data consists of accurate force and moment measurements on a water-cooled sting-mounted model at 2.1% scale. The heating data is derived from a thermographic phosphor imaging technique[16,17] using models at 2.1% and 3.6% scale. The original goal of this numerical effort was to validate the GASP code against the aerothermal heating data. It was realized, however, that the solutions contain the information needed to compute the aerodynamic coefficients, thus an effort is made to compare against selected aerodynamic data.

Table 1. Summary of test facilities.

Facility	Test Gas	Data
20-Inch Mach 6	Air, γ=1.4	Aerodynamic, Heating
20-Inch Mach 6	CF_4, γ=1.1	Aerodynamic
31-Inch Mach 10	Air, γ=1.4	Aerodynamic, Heating
22-Inch Mach 20	He, γ=1.67	Aerodynamic

Aeroheating Validation Exercises

To accomplish the aeroheating validation, computational simulations are compared with the heating data derived from the thermographic phosphor technique[16,17] in the NASA Langley 31-Inch Mach 10 facility. Several conditions were selected from a large matrix of runs, and the conditions corresponding to one of these is shown in Table 2. The case is representative of the angle-of-attack, body-flap, setting and Reynolds number expected during entry. The model tested is the 2.1% scale Rev 3.1 geometry.

Table 2. 31-Inch Mach 10 air facility run conditions.

Run	α, deg	δ_{bf}, deg	M_∞	Re_∞, x10^6, ft^{-1}
37	40	25	9.8	1.11

Comparison with aeroheating data

Figure 7 shows a comparison of the experimental and numerical results. The image contains global values of the non-dimensionalized heat transfer coefficient h/h_{ref}. The comparison shows the features and trends observed in the experimental image to be captured well by the computational simulation. The experimental data does not permit comparison near the stagnation region due to fluorescence quenching where the model surface temperature exceeds the phosphor calibration limits. The only visible discrepancy between the data and the CFD is in the flap region, where the CFD is slightly lower. It was assumed that the flow was laminar in the reattachment region at the Reynolds number of this test. If the flow is transitional or turbulent the heating would be higher. The calculations assumed the flow to be laminar.

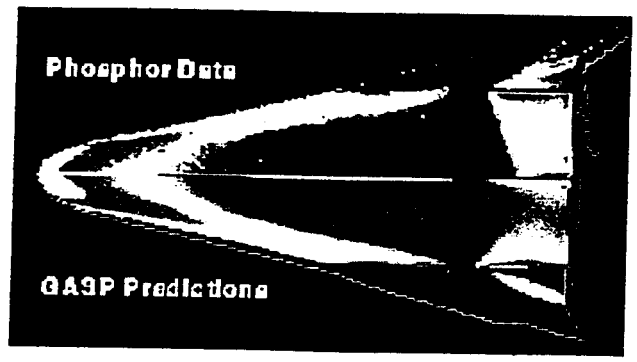

Figure 7. Comparison of Experimental and Computational Results.

The quantitative experimental data obtained from post-processing of the image, in terms of normalized heat transfer coefficient (h/href), was provided at specific cross sections and along longitudinal sections. To compare with the experimental heat-transfer coefficient, it is necessary to post-process the CFD data in a similar manner to the experimental data reduction. Details of this process to produce comparable CFD and experimental quantities are provided in Appendix A. Figure 8 shows the orientation of the camera, a cutting plane at x/L=0.5, and the model. For the run presented, the camera angle is 28 deg.

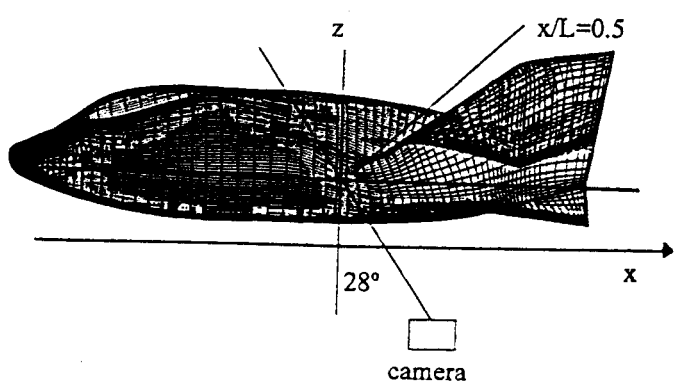

Figure 8. Side view of CFD mesh, showing cut lines at x/L=0.5.

The longitudinal comparison of h/h_{ref} at a station slightly off from the bi-symmetry plane (y/L = 0.05) is shown in Fig. 9a. A solution comparison along the line of symmetry (y=0.0) is very similar to the comparison shown in Fig. 9a except that the flow separation and the reattachment is different due to the split flap geometry. The cut line, y/L=0.05, passes through the flap and the reattachment on the deflected flap and thus allows comparisons. The overall agreement is generally within the experimental uncertainty, estimated to be around ± 15%. Slight disagreement occurs between x/L=0.75 and x/L=0.85, where the computational predictions appear to be deficient in capturing the flow details due to streamwise flow separation. The heating prediction is slightly low in the flap region where the heating is higher due to flow reattachment.

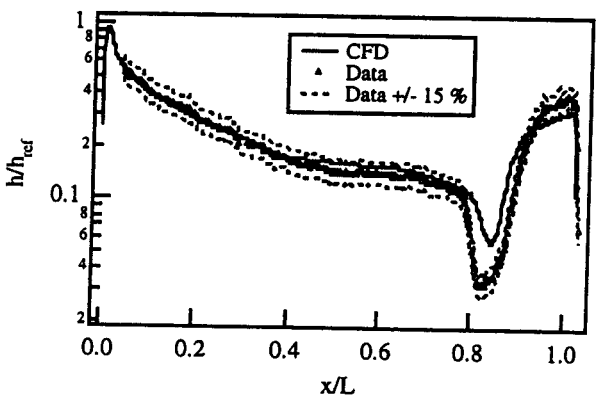

Figure 9a. Comparison of experimental data and CFD at a longitudinal station of y/L=0.05.

Representative comparisons at three different axial cuts are shown in Figs. 9b, 9c and 9d. The comparison at axial cut x/L = 0.25 and at x/L = 0.73 demonstrate the very good agreement between the prediction and the measurements. The experimental data show slight asymmetry and the two curves represent the data from the left and the right side. The computational data are symmetric.

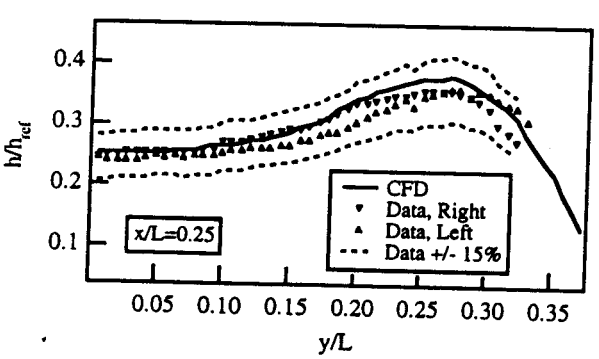

Figure 9b. Comparison of test data and CFD at an axial station of x/L=0.25

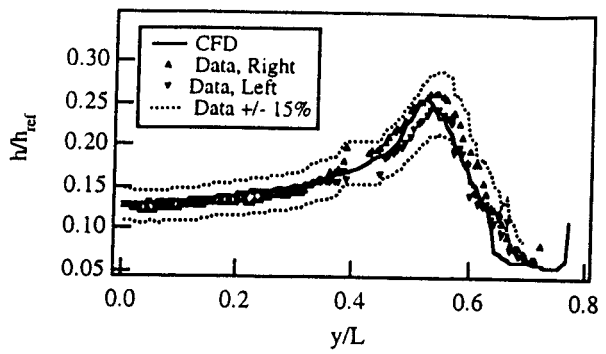

Figure 9c. Comparison of test data and CFD at an axial station of x/L=0.73.

The comparison at x/L = 0.95 is the last available section where the line cut passes through large geometric changes and the remarkable agreement in such a geometrically complex region lends confidence to the simulation.

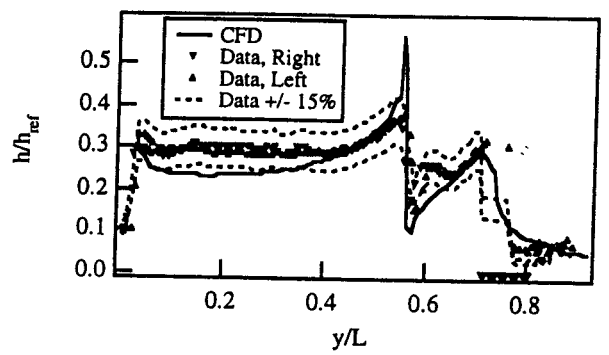

Figure 9d. Comparison of test data and CFD at an axial station of x/L=0.95.

Aerodynamic Predictions

The aerodynamic data base is obtained from the experimental measurements made in the NASA Langley 22-Inch Mach 20 Helium tunnel, the 20-Inch Mach 6 Air tunnel, and the 20-Inch Mach 6 CF4 tunnel. Computational simulations are performed for the conditions in Table 3 to estimate the accuracy of the predictions and to assess the extrapolation of the wind tunnel data to the full scale flight vehicle. The wind tunnel models are 2.1% scale Rev. 3.1 geometry.

Table 3. Test Conditions for the Aerodynamic Cases

Runs	Mach	Test Gas	$Re_{\infty,L}$ x10^6
32	19.5	He	3.0
70, 71, 76, 77	5.9	Air	0.6 - 2.1

Comparison to Mach 20 helium wind tunnel data
Aerodynamic data are measured in the Mach 20 helium wind tunnel for a range of angles of attack and body-flap settings. While the base pressure is typically low for hypersonic vehicles, its contribution to the axial

force must be considered in order to model the axial force coefficient more accurately. As shown in Fig.10, the base pressure coefficient measured in the experiment is approximately the mean value calculated for the windward and leeward sides. The base pressure was measured at two locations near the sting.

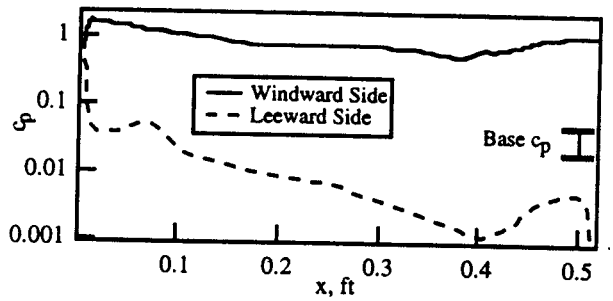

Figure 10. Comparison of calculated symmetry plane pressure coefficent to measured base pressure coefficient.

Figure 11 compares the calculated and measured axial force coefficients for a range of angles of attack. Once the computed solution includes the correction for the average base pressure, the agreement is quite good. Ref. 3 contains a discussion of the data uncertainty, which is generally smaller than the size of the symbols on the plots.

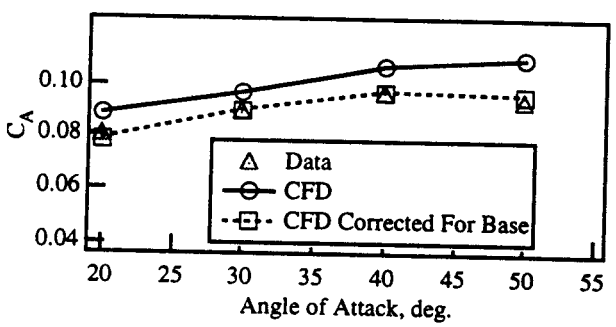

Figure 11. Axial force coefficient comparison, Mach 20 helium wind tunnel case.

The comparison with the normal force is shown in Fig. 12 without any base correction. The comparison is good since the projected base area is small in this direction.

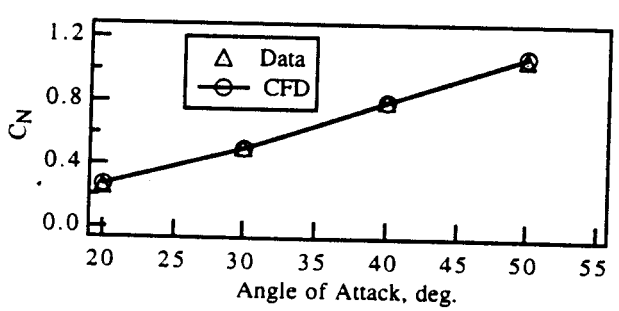

Figure 12. Normal force comparison, Mach 20 helium wind tunnel Case.

The comparison with the pitching moment is shown in Fig. 13. Without the base correction, the predicted pitching moment is more positive than the data indicates. No attempt was made in the figure to correct the computed solution for the base pressure contribution since the base pressure was measured at only one z location in the experiment. If a correction was made and the moment applied at the base centroid, the agreement would be actually worse. It is expected that the base pressure should vary from a higher value near the windward side to a lower value near the leeward side, thereby shifting the moment center downward in comparison to an area centroid correction and possibly bringing the comparison into better agreement. Plans are underway to include the base effect in the computations.

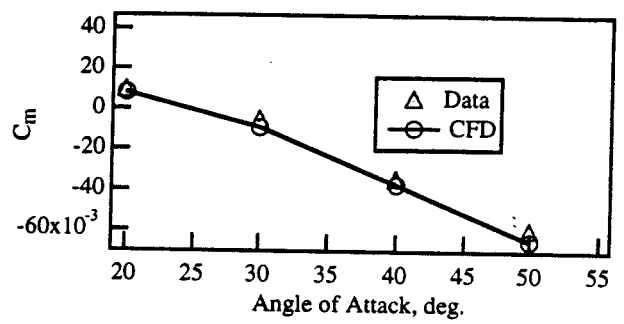

Figure 13. Pitching moment comparison, Mach 20 helium wind tunnel case.

Comparison to Mach 6 Air Wind Tunnel Results

The aerodynamic characteristics dependence as a function of Reynolds number is shown in Figs. 14a and 14b. The data show a gradual decrease in axial force coefficient and pitching moment with Reynolds number. The decrease in axial force is attributable to the decrease in skin friction drag coefficient with Reynolds number and also the effect of Reynolds number on the size of the separated region ahead of the flap and subsequent reattachment. The CFD solutions show a similar trend and compare in absolute value except for the lowest Reynolds number when corrected for the base pressure.

For the pitching moment, which is uncorrected for base effects, the predictions are better at higher Reynolds number. This seems to make sense since the measured base pressure coefficient decreases with Reynolds number. The lack of base flow modeling in the computations is suspected to be the major cause of the discrepancy and with improved modeling the predictions are expected to be better.

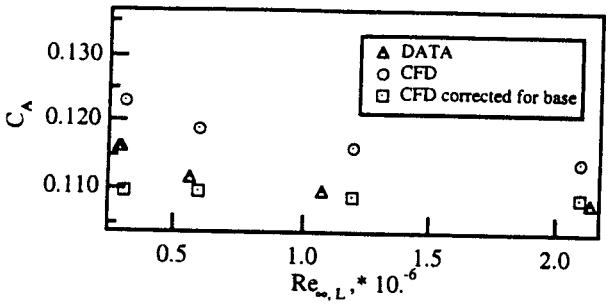

Figure 14a. Effect of Reynolds number on axial force coefficient moment, Mach 6 air wind tunnel data.

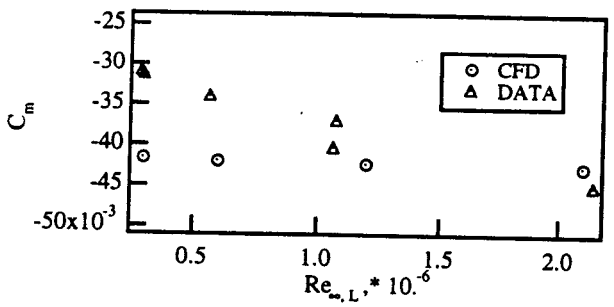

Figure 14b. Effect of Reynolds number on pitching moment, Mach 6 air wind tunnel data.

Flight Cases

The Cycle 5 trajectory is shown in Fig. 15, which corresponds to the Rev 3.1 geometry with a vehicle weight of 20,000 lbs. The entry duration is about 1600 seconds, with an 800-second period of nearly uniform heat flux. Shown in the figure is the stagnation point heat transfer to a 1-foot diameter, cold wall reference sphere calculated using the Fay-Riddel method. The level of heat transfer during the peak heating phase is near the maximum allowable for single-use, high-density TUFI-coated space shuttle tiles.

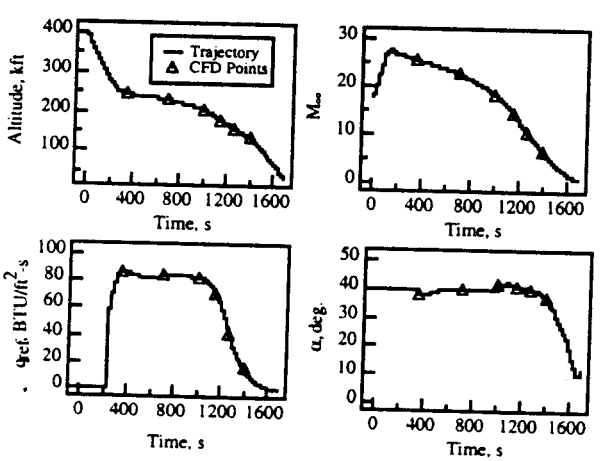

Figure 15. Cycle 5 trajectory.

Five points from the trajectory profile are initially chosen for calculations and are shown in Table 4. The cases are all run at an angle of attack of 40 deg and a body flap setting of 25 deg. At these conditions, a fully catalytic radiative equilibrium boundary condition with an emissivity of .85 is assumed for the wall on the entire geometry. In a separate computation, the nose region alone is modeled with the catalycity/emissivity corresponding to TUFI-coated tiles, which is the baseline TPS material.

Table 4. Flight Cases.

Time, s	Alt., kft	M_∞	α, deg	δ_{bf}, deg	$Re_{\infty,L}$ x10^6
354	242.5	25.5	40	25	.188
715	228.6	22.5	40	25	.296
1003	204.6	18.5	40	25	.655
1151	179.3	14.5	40	25	1.51
1271	157.0	10.5	40	25	2.35
1400	134	6.68	40	25	3.90

Aerothermodynamic Heating

The results of the Mach 25.5 case with the fully-catalytic wall boundary condition are shown in Fig. 16. The vehicle geometry is a 120% scaled Rev 3.1 configuration. The grid is clustered near the wall, with a wall spacing of 10 microns at the nose and 30 microns near the tail. This is found to produce a temperature jump on the order of 20 °R which is considered sufficient for a grid independent solution. It is seen that the nose of the vehicle gets extremely hot (above 3000 °F). This temperature is above the single use limit of shuttle tiles and may lead to tile slumping. It should be noted that this calculation is performed with a fully-catalytic wall boundary condition, which is often used in the design process to ensure conservatism. Based on the above validation exercise and other validation work related to the Space Shuttle,[7] it is estimated that the predicted temperatures are accurate to within ±25 deg R over most regions of the vehicle.

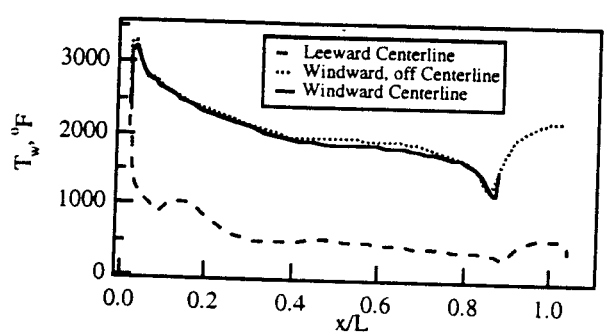

Figure 16. Temperature vs. x/L, Mach 25.5 case.

The computed surface temperatures using the fully-catalytic boundary condition are compared with the results obtained using the catalytic value corresponding

to TUFI-coated tiles as shown in Fig. 17. The peak temperatures are seen to decrease on the order of 100 °F but are still at the limit of single use TUFI tiles over a small region near the nose. In the current modeling, the in-depth conduction loss is neglected and this adds conservatism as well. This is expected to allow the nose cap temperature to be near the material limit.

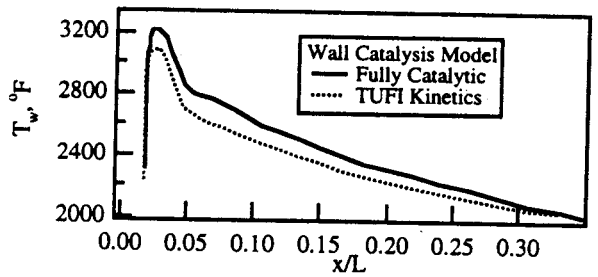

Figure 17. Windward centerline comparison of fully catalytic and TUFI kinetics boundary condition.

Real-Gas Effects on Aerodynamics

Real-gas effects on aerodynamics typically manifest through an increased pressure ratio across the shock wave. This is because at high Mach numbers, the temperature downstream of the shock wave is high and air no longer behaves as a perfect gas with γ=1.4. Excitation of the vibrational modes leads to a reduction in γ, which increases the pressure ratio. This is demonstrated in Figs. 18a and 18b, which shows the pressure coefficient on the windward side. In the nose region, the pressure coefficient is higher for the real-gas calculation, causing a nose up increment in the pitching moment. In the body-flap region, there is a substantial increase in the pressure, making the flap more effective and causing a net nose-down increment. The overall effect for this body flap setting (δ_{bf}=25 deg) is a more restoring, or negative, increment in the pitching moment.

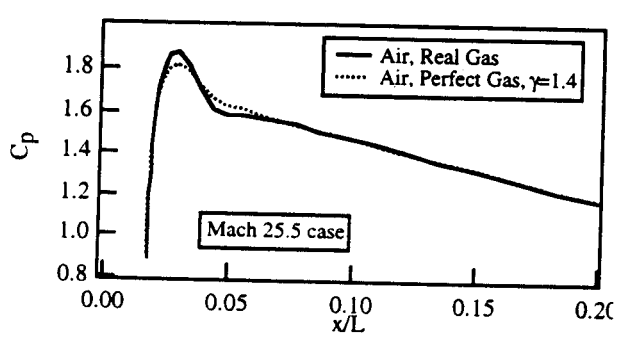

Figure 18a. Real gas effects on pressure coefficient near the stagnation point.

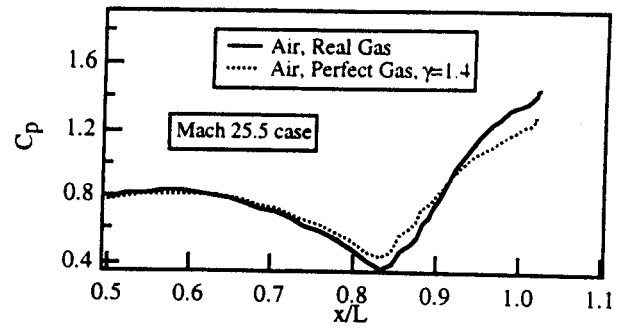

Figure 18b. Real gas effects on pressure coefficient near the body flap.

This trend is supported by the experimental data from the Mach 6 CF4 (γ=1.1) and air (γ=1.4) facilities.[4] The data show a similar change in the pitching moment between the two test gases. For lower body-flap settings however, the increased flap effectiveness no longer compensates for the increase at the nose and the net increment is positive. This is consistent with the initial space shuttle flights which exhibited a significant difference from perfect-gas wind tunnel predictions in pitching moment.[6]

The overall effect on the aerodynamic coefficients is shown in Figs. 19-21. Perfect gas cases with a constant wall temperature of 540 °R were computed at the flight conditions for comparison. The computed wind tunnel cases for the Mach 6 air and the Mach 20 helium runs are also plotted.

In Fig. 19, the axial force coefficient is seen to decrease as the Mach number decreases. This is largely due to a decrease in the skin friction drag with Reynolds number, which increases by an order of magnitude between Mach 25 and Mach 6, as shown in Table 4. The difference between the perfect-gas and real-gas calculations decreases as the Mach number decreases, as expected. The difference between the perfect gas and real gas is largely due to the increased flap effectiveness. The Reynolds number for the Mach 6 air wind tunnel case is similar to the Mach 6 flight case and produces a similar axial force coefficient.

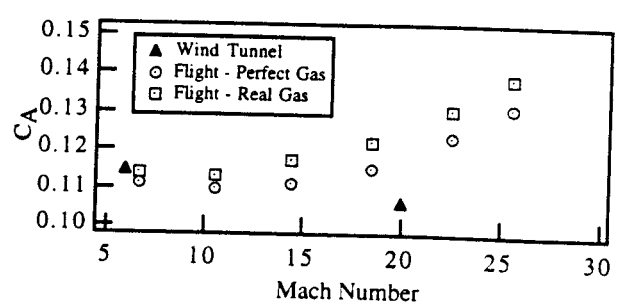

Figure 19. Real-gas effects on axial force coefficient.

In the normal force comparison shown in Fig. 20, a similar behavior is seen between the perfect-gas and real-gas calculations, once again attributable largely to the increased flap effectiveness. The Reynolds number effect is much less since the skin friction drag component of the normal force is small.

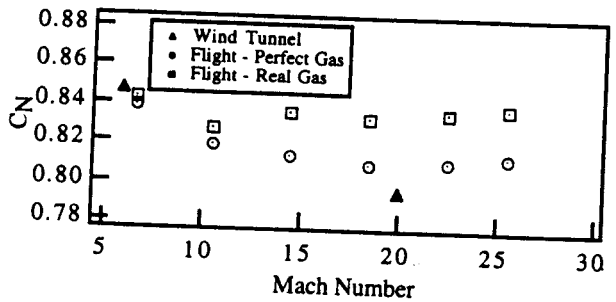

Figure 20. Real-gas effects on axial force coefficient.

The effect on the pitching moment is shown in Fig. 21. As stated before, the body flap is more effective due to real-gas effects, causing a more negative pitching moment. This behavior begins to disappear at Mach 10 when air behaves more like a perfect gas.

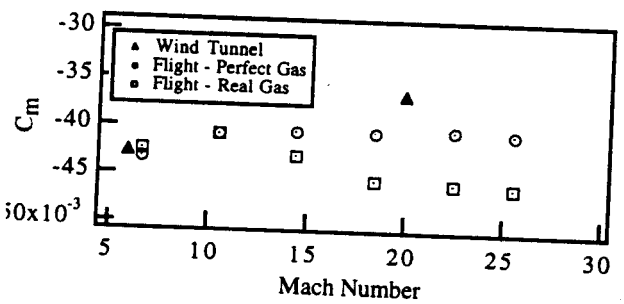

Figure 21. Real-gas effects on moment coefficient.

Concluding Remarks

Validation of the GASP code has been performed for the X-38 geometry. Comparisons of aerodynamic heating predictions with wind tunnel data were generally within the expected ±15% accuracy of the data. The aerodynamic forces and moment comparisons are also found to be reasonably good. The base effect needs to be included in the computation in order to match the data. Predictions of surface temperatures to the flight vehicle were made and were estimated to be accurate to ±25 deg R. Real gas effects on the aerodynamic coefficients were investigated. The computational code runs sufficiently fast to provide complete trajectory-based calculations required to map out appropriate TPS materials, and to provide input for TPS sizing calculations.

Acknowledgments

The work of the second and third authors which was supported by the Reacting Flow Environments Branch of NASA Ames Research Center through a Contract NAS2-14031 to ELORET is gratefully acknowledged. The authors would also like to thank Ron Merski of NASA Langley for the thermal phosphor data and Dinesh Prabhu of Thermosciences Institute for his modifications to the GASP code.

References

1. Campbell, C. H., Caram, J. M., Li, C. P., and Madden, C. B., "Aerothermodynamic Environment Definition for an X-23/X-24A Derived Assured Crew Return Vehicle," AIAA Paper 96-1862.

2 Venkatapathy, E., Prabhu, D., Loomis, M., Polsky, S., Papadopoulos, P., and Davies, C. B., "X33 Aerothermal Environment Simulations - A Critical Look at the Design and CFD Requirements including Special Topics", Abstract submitted to the 36th AIAA Aerospace Sciences Meeting, Reno, NV, 1998.

3. Campbell, C. H., Caram, J., Berry, S., DiFulvio, M., and Horvath, T., "Overview of X-38 Hypersonic Wind Tunnel Data and Comparison with Numerical Results," AIAA Paper 97-0567.

4. Campbell, C. H., Caram, J., Berry, S. and Horvath, T., "An Overview of XCRV Hypersonic Aerothermodynamic Wind Tunnel Data and Comparison With Numerical Results," AIAA Paper 97-2475.

5. Berry, S. A., Horvath, T. J., Robach, V. E., and Williams, G. B. Jr., "Results of the .0362-Scale X-38 (Rev. 3.1) Vehicle Aerothermodynamic and Boundary Layer Transition Test in the NASA Langley 20-Inch Mach 6 Tunnel," NASA TM 112857, 1997.

6. Brauckmann, G. J., Paulson, J. W. Jr., and Weilmuenster, K. J., "Experimental and Computational Analysis of Shuttle Orbiter Hypersonic Trim Anomaly," *Journal of Spacecraft and Rockets*, Vol. 32, No. 5, 1995.

7. Olynick, D. R., and Tam, T., "Trajectory-Based Validation of the Shuttle Heating Environment," *Journal of Spacecraft and Rockets*, Vol. 34, No. 2, 1997.

8. "GASP v3.0 User's Manual," Aerosoft Inc. 1996.

9. Park. C., "Review of Chemical-Kinetic Problems of Future NASA Missions, I: Earth Entries," *Journal of Thermophysics and Heat Transfer*, Vol. 7, No. 3, 1993.

10. Wilke, C. R., "A Viscosity Equation for Gas Mixtures," *Journal of Chemical Physics*, Vol. 18, No. 4, 1950, pp. 517-519.

11. Blottner, F. G., Johnson, M., and Ellis, M., "Chemically Reacting Viscous Flow Program for Multi-Component Gas Mixtures," Sandia Labs., Rept SC-RR-70-754, Albuquerque, NM Dec. 1971.

12. Stewart, D. A., Pallix, J., and Esfahani, L., "Surface Catalytic Efficiency of Candidate Ceramic Thermal Protection Systems for SSTO," NASA CDTM-20007, March 1995.

13. Steinbrenner, J. P., and Chawner, J. R., "The GRIDGEN Version 9 Multiple Block Grid Generation Software Package," MDA Engineering Report 94-01, June 1994.

14. Chan, W. M., Chui, I. T., and Buning, P. G., "User's Manual for the HYPGEN Hyperbolic Grid Generator and the HGUI Graphical User Interface," NASA TM 108791, 1993.

15. Davies, C. B., and Venkatapathy, E., "The Multidimensional Self-Adaptive Grid Code SAGEv2," NASA TM 110350, 1995.

16. Merski, N. R., "A Relative-Intensity Two-Color Phosphor Thermography System," NASA TM 104123, 1991.

17. Merski, N. R., "An Improved Two-Color Relative-Intensity Phosphor Thermography Method for Hypersonic Wind Tunnel Aeroheating Measurements," Ph.D. Dissertation, George Washington University, 1997.

Appendix A: Data Reduction for Heating Comparison

The reduced experimental data were given in spreadsheet format, providing numeric values of the normalized heat transfer coefficient at specified cross sections (x) and at specified longitudinal sections (y) of the vehicle geometry. Due to the nature of the experimental set-up and data reduction procedure, three issues had to be resolved before valid comparisons could be made: 1) consistent units; 2) location of comparison stations; and 3) definition of camera angle.

1) The specified experimental cross-section locations were transformed to the CFD unit of feet, measured from the system origin and at 2.1% scale, to give the location along the vehicle centerline. The experimental flow values were given in terms of the heat transfer coefficient, h/h_{ref} and the GASP computed heat flux values were defined in fps units. The GASP results were then converted to h/h_{ref}

2) The side view of the CFD surface grid is given in Fig. 8, where the vehicle centerline joins the nose to the tail. Although this line is not quite parallel to the x-axis, it was assumed to be parallel. The figure shows an example of an experimental data station at x/L_x=.5 where L_x =282.5", i.e. halfway between the nose and tail, lying on the centerline. The transformation from the experimental x station (x_e) to the CFD x station (x_c) is given by $x_c=(x_e*282.5+5)*0.021/12$. The experimental longitudinal stations were normalized with respect to the wing span, given as L_y=86.75", producing $y_c=y_e*0.021*86.75/12$.

3) The experimental data lies on the surface of the cut plane emanating from the camera shown in Fig. 8, at an angle of 28° to the x axis. A constant CFD cut plane at x/L=0.5 would be perpendicular to the x axis as shown. Each x location on the computational plane was transformed with respect to the camera angle giving $x_n=x_c\cos 28+z_c\sin 28$. The y locations needed no transformation to compensate for camera angle.